

Lawrence Berkeley National Laboratory

Chemical Sciences

Title

Colloidal 2D-0D Lateral Nanoheterostructures: A Case Study of Site-Selective Growth of CdS Nanodots onto Bi₂Se₃ Nanosheets

Permalink

<https://escholarship.org/uc/item/9mb4g2fv>

Journal

Nano Letters, 15(6)

ISSN

1530-6984

Authors

Xu, Biao
Li, Haoyi
Yang, Hao
et al.

Publication Date

2015-06-10

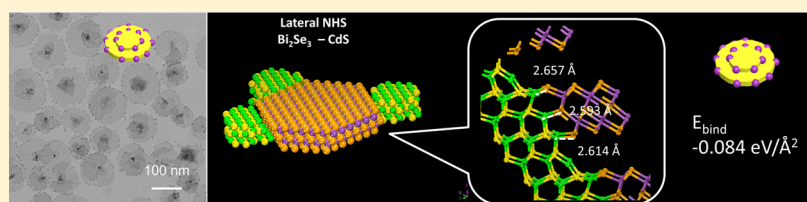
DOI

10.1021/acs.nanolett.5b01464

Peer reviewed

Colloidal 2D–0D Lateral Nanoheterostructures: A Case Study of Site-Selective Growth of CdS Nanodots onto Bi₂Se₃ NanosheetsBiao Xu,^{†,§} Haoyi Li,[†] Hao Yang,[‡] Wentian Xiang,[†] Gang Zhou,[⊥] Yue Wu,^{*,§} and Xun Wang^{*,†}[†]Department of Chemistry and [‡]Department of Materials Science and Engineering, Tsinghua University, Beijing 100084, China[§]Department of Chemical and Biological Engineering, Iowa State University, Ames, Iowa 50010, United States[⊥]State Key Laboratory of Chemical Resource Engineering, Beijing University of Chemical Technology, Beijing 100029, China

S Supporting Information



ABSTRACT: Two-dimensional (2D) nanoheterostructure (2D NHS) with nanoparticles grown on 2D nanomaterial substrates could potentially enable many novel functionalities. Controlled site-selective growth of nanoparticles on either the lateral or the basal directions of 2D nanomaterial substrates is desirable but extremely challenging. Herein, we demonstrate the rational control of lateral- and basal-selective attachment of CdS nanoparticles onto 2D Bi₂Se₃ nanosheets through solution phase reactions. The combination of experimental and theoretical efforts elucidate that site-relevant interfacial bonding and kinetic control of molecular precursors play vital roles for site selectivity. Furthermore, the electronic structures revealed from density functional theory calculations explain the superior performance of the lateral 2D NHSs compared to their basal counterpart in prototype photoelectrochemical cells. The present study will inspire the construction of other site-selective 2D NHSs with well-defined structure and unique properties.

KEYWORDS: Nano, two-dimensional, heterostructure, density functional theory, site-selective

In the past decade, two-dimensional (2D) nanostructures have attracted significant interest due to their superior performances and potential applications in electronics and optoelectronics.^{1–3} By the integration of functionalities and evolution of new attributes, emerging nanoheterostructures (NHSs) based on 2D materials⁴ are expected to hold important advantages over those based on conventional host materials. In the realm of NHSs, site selectivity is an intriguing and important topic that leads to unprecedented architectures and spatially modulated properties.⁵ The layered structure and crystallographic anisotropy of 2D materials in nature render the site-preference, basal (vertical) or lateral, in 2D NHSs, different from that in 0D and 1D NHSs. While there has been a lot of progress in the development of site-selective 0D⁶ and 1D⁷ NHSs, only a few basal NHSs have been studied in terms of van der Waals (vdW) heteroepitaxy,^{8,9} in which the disparate 2D layers were connected by the vdW force.¹⁰

On the other hand, several experimental^{11,12} and theoretical¹³ studies revealed that the finite but active lateral planes have the potential to initiate heterogeneous nucleation and growth, simultaneously allowing for versatile functionality. This implies that the controlled synthesis of lateral 2D NHS is not only feasible, but also attractive. Nonetheless, the progress is limited to those between two 2D compounds with the same crystal structure symmetry and bonding characteristics by gas-

phase epitaxy.^{14,15} In these cases, the interfacial bonding was relatively simple, and the lattice mismatch was trivial. In principle, materials with different space groups, if integrated into 2D NHS, could provide an opportunity to diversify the functionalities, but it imposes great challenges for the synthesis due to the complex and unamiable interfacial bonding. Apart from the thermodynamic limitation, the kinetic factors also affect the growth style of 2D NHSs in synthetic attempts. To date, comprehensive studies including site selectivity of 2D NHSs are still at the early stage due to the structural complexity and synthetic uncertainty. Hence, gaining insights into the interfacial bonding at the atomic level and further manipulating the reaction kinetics of the synthesis would assist the rational control of the site selectivity between 2D materials and other nanomaterials.

Herein, we demonstrate a breakthrough in the site-selective growth of 2D NHS. We choose 2D lamellar V–VI Bi₂Se₃ (*R* $\bar{3}m$) and 0D II–VI wurtzite CdS (*P* $\bar{6}_3mc$) as the functional building blocks to construct the 2D NHS, which breaks the limitations in material choice of crystal structure symmetry and dimensionality. Layered Bi₂Se₃ has recently been revisited in

Received: April 15, 2015

Revised: May 20, 2015

Published: May 29, 2015

physics and materials science as a topological insulator,¹⁶ where a single Dirac cone on the surface and a relative large gap (0.3 eV) would make Bi_2Se_3 a good choice for spintronic and superconducting devices.^{17,18} Meanwhile, wurtzite CdS has been adopted for optoelectronic, photoelectrochemical, and photocatalytic applications.¹⁹ We show that both 2D Bi_2Se_3 –CdS lateral and basal (vertical) NHSs can be selectively synthesized via a colloidal route under rational control based on the reaction kinetics.

In our synthesis, Bi_2Se_3 nanosheets (NSs) with two different surface compositions are used as seeds²⁰ for the heterogeneous nucleation and growth of CdS nanoparticles (NPs). The details of the syntheses are described in the Supporting Information. For surface-stoichiometric Bi_2Se_3 NSs (sample 1), through the choice of precursors with different reactivity (see conversion rates depicted in Table S1 of the Supporting Information), different site selectivity could be achieved (Figure S1). For example, CdS NPs mainly grow laterally using sodium diethyldithiocarbamate²¹ (DDTC) as an inert sulfur precursor (see Table S1, line 1; Figure S1a). By contrast, CdS NPs could be grown basally onto the surface-stoichiometric Bi_2Se_3 NS using thiourea (Figure S1b) or thioacetamide (Figure S1c) as active precursors (see Table S1, lines 3 and 4, respectively). However, for surface-Se-rich Bi_2Se_3 (sample 2), laterally selective growth is preferred in most of the cases. For example, S precursors like inert DDTC and reactive thiourea both lead to the lateral growth of CdS NPs on the surface-Se-rich Bi_2Se_3 NSs shown by transmission electron microscopy (TEM) studies (Figure 1a, Figure S2a (sample 2–1, using DDTC), and Figure S2b (using thiourea)) and high-angle annular dark-field scanning transmission electron microscopy (HAADF STEM) (Figure 1b, sample 2–1). To achieve the basal growth mode, the most reactive thioacetamide must be used as precursor (Sample 2–4, Figure 1e, Figure S2c, and Table S2). The Bi_2Se_3 NSs show a multilayered structure with steps, and the steps are clearly visualized in the HAADF STEM studies with enhanced contrast (Figure 1b). Both the lateral surfaces and the inner steps are decorated with CdS NPs. The elemental distribution is clearly shown by energy dispersive spectroscopy (EDS) mapping (Figure 1b, insets). The high resolution TEM (HRTEM) studies show the single crystal lattice fringes of CdS and Bi_2Se_3 in both the basal (sample 2–4, Figure S11c) and lateral NHSs (sample 2–1, Figure 1c). The ratio of Bi–Cd in the NHSs can be tuned in a wide range (sample 2–2 and 2–3, Figure S3). Further tuning of these NHSs (samples 3, 4, 5, and 6) (Figures S4 and S5) relies on judicious control of the synthetic parameters such as reducing reagents, precursor concentrations, and additives.

The structure of the lateral NHS is further characterized by various approaches. The morphology is inspected by scanning electron microscopy (SEM) (Figure S6). The thickness is measured to be less than 6 nm (corresponding to six quintuple layers) by atomic force microscopy (AFM) (Figure S7). Crystal phases of both the segments (Bi_2Se_3 , JCPDS 33–0214, space group: $R\bar{3}m$; CdS, JCPDS 65–3414, space group: $P6_3mc$) can be indexed by the powder X-ray diffraction (XRD) (Figure S8). The characteristic Raman peaks of Bi_2Se_3 (A_{1g}^1 , E_g^2 , and A_{1g}^2) and CdS (LO) can be observed in good agreement with the literature^{22,23} (Figure S9). Inductively coupled plasma atomic emission spectroscopy (ICP-AES) confirms the atomic compositions of Bi_2Se_3 and CdS in each sample (Table S3). X-ray photoelectron spectroscopy (XPS) has been conducted to study the chemical environment of each element (Figure

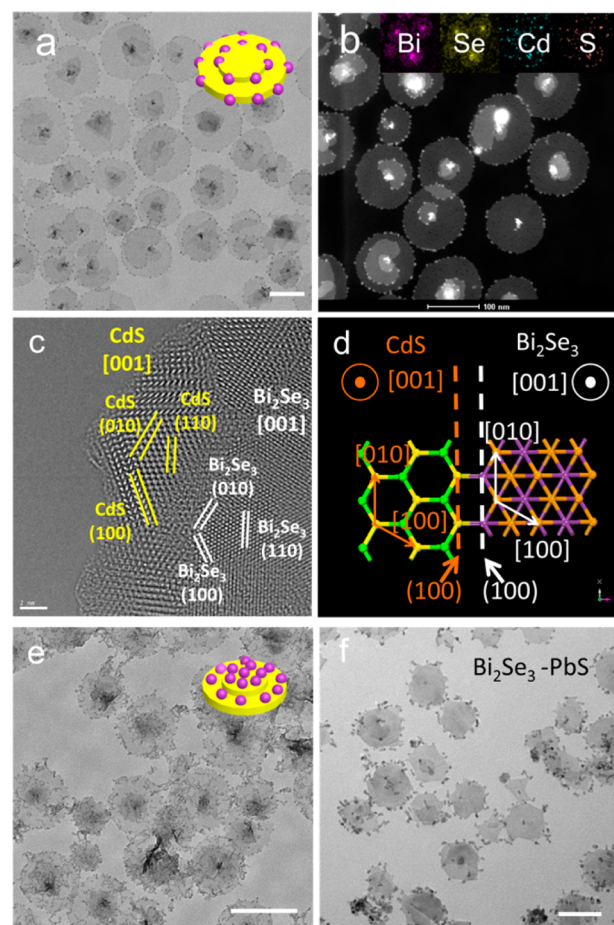


Figure 1. (a) TEM (scale bar 100 nm) and (b) HAADF STEM image (scale bar 100 nm) of the lateral 2D NHS made from Bi_2Se_3 NSs–CdS NPs (sample 2–1); the insets in panel b show the element mapping. (c) HRTEM image (scale bar 2 nm) and (d) atomic model of the Bi_2Se_3 –CdS interface in sample 2–1, viewed along the [001] axes. (e) TEM (scale bar 100 nm) image of basal Bi_2Se_3 –CdS NHS (sample 2–4). (f) TEM (scale bar 100 nm) image of lateral Bi_2Se_3 –PbS NHS showing the compatibility of our synthesis method for other 2D NHS systems.

S10). Surface compositions of the surface-stoichiometric (sample 1) and surface-Se-rich (sample 2) NHSs are confirmed by surface-sensitive XPS quantitative analysis (Figure S10).

Notably, HRTEM studies disclose the interesting orientation relationship between Bi_2Se_3 and CdS at the single-NHS level, which set the basis for further theoretical modeling. It is found that the 001 axes of Bi_2Se_3 and CdS are aligned with each other (Figure S11a, fast Fourier transform (FFT) patterns in the insets) and with the normal direction of the Bi_2Se_3 nanosheets. Furthermore, the (100), (010), and (110) lattice fringes of Bi_2Se_3 are also parallel to those of CdS, respectively (Figure 1c, S11a for lateral NHS and S11c for basal NHS). Importantly, we also obtain a direct observation of the in-plane view of the lateral NHS that shows the (001) \parallel (001) parallel relationship between Bi_2Se_3 and CdS (Figure S11b), demonstrating the interesting epitaxial growth behavior of CdS on Bi_2Se_3 . Actually, the lattice constants along the x axis of CdS and Bi_2Se_3 are the same ($a = 4.14 \text{ \AA}$), and the aob planes are both hexagonal. This implies the perfect match of the honeycomb-like 2D sublattices (basal planes) of these two constituents (Figure 1d). However, along the lateral facets, the coordination shells do not match

well (Figures S12 and S13), which might lead to the complex interfacial bonding, as will be stated in the following section on the density function theory (DFT) calculations.

To further understand the mechanism of the site selectivity, we construct a series of atomic models (see Supporting Information, section 3) for CdS–Bi₂Se₃ NHSs based on experimental observations (HRTEM (Figure 1c and Figure S11) and XRD (Figure S8)) and perform DFT calculations on the interfacial bonding and stability. Three interface structures are proposed to stem from different site-selective growth (Figure 2). Thermodynamically, as evident from the binding

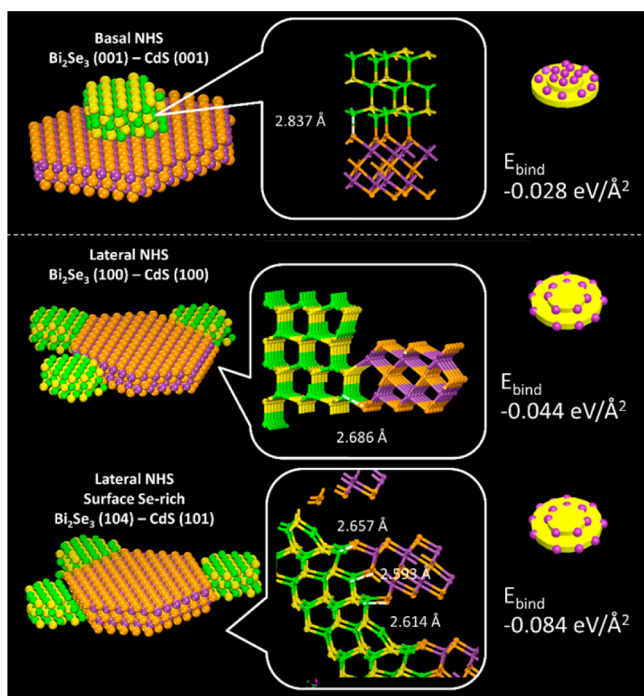


Figure 2. Different atomic models after DFT calculations: basal and lateral NHSs. The binding energies and bonding lengths of different interfacial models are shown. The green, yellow, purple, and orange balls correspond to the Cd, S, Bi, and Se atoms, respectively.

energy, Se-rich lateral growth (Bi₂Se₃ (104)–CdS (101)) is the most preferable, followed by surface-stoichiometric lateral growth (Bi₂Se₃ (100)/(110)–CdS (100)/(110)), and finally basal growth (Bi₂Se₃ (001)–CdS (001)). More precisely, the electron density difference (Figure S28a) and larger interfacial Cd–Se bond length (2.837 Å) than that of the CdSe bulk (2.620 Å) are indicative of vdW interaction (–0.028 eV/Å², Figure S15) in basal bonding,¹⁰ resembling the case of vdW heteroepitaxial NHSs. This is ascribed to the topmost coordination-saturated Se_{3c} atoms of Bi₂Se₃ nanosheets. While surface-stoichiometric and Se-rich lateral connections involve partial and full saturations of dangling bonds of lateral Se/Bi atoms with slightly long and nearly standard Cd–Se/S–Bi bonds, respectively, both show chemical bonding. The difference is due to the different lattice and valence match. This also indicates that the surface atomic composition is very important for site selectivity, as observed in our synthesis. According to classical heterogeneous nucleation theory,^{24,25} the site selectivity and preferred growth mode of NHSs is controlled by the thermodynamic and kinetic barriers of nucleation. Further combining our experiments (Figure S1 and Table S1) with calculations, we can see that the thermodynamic

ally controlled scenario is present in inert and mild sulfur precursors (DDTC and thiourea), in which nucleation reaction is relatively slow (Table S1). However, the kinetically controlled scenario dominates the synthesis using active sulfur precursor (thioacetamide), where oversaturation of Cd and S atoms in solution is quickly reached at the initial stage of the reaction (Table S1), and then the possibility of CdS to deposit onto the basal or lateral plane of Bi₂Se₃ is nearly the same²⁶ because the large basal plane has more anchoring site. Mild sulfur precursor (thiourea) data show that the criteria of energy difference that may lead to a thermodynamically preferable growth mode is 0.056 eV/Å², twice the binding energy of basal growth.

On the basis of the controlled synthesis of Bi₂Se₃–CdS lateral NHSs and the understanding of the interfacial bonding and growth mechanism, we extended Bi₂Se₃ to a series of isomorphous V–VI layered chalcogenides with different lattice parameters, such as Bi₂Te₃, Bi₂Te₂Se, and Bi₂TeSe₂ (Figure S23), and lateral growth of CdS is again achieved. Moreover, we find that wurtzite CdSe NPs could also be deposited laterally onto Bi₂Se₃ NSs (Figure S24), which is not surprising as they are isomorphous with CdS. Besides the wurtzite family, other types of metal chalcogenide could also be accommodated onto the lateral sites of Bi₂Se₃ NSs, as exemplified by rocksalt (fcc NaCl-like) PbS (Figure 1f and Figure S25). Rock Salt PbS (fcc NaCl-type) with hexagonal honeycomb structure along its 111 axis is investigated (Figure 1f and Figure S25). The Bi₂Se₃ NS is synthesized according to the procedure for sample S, and the Pb and S precursors are lead acetate and thioacetamide. Both XRD (Figure S25b) and HRTEM (Figure S25c) confirm the components of Bi₂Se₃ and PbS. The view along PbS (111) plane and Bi₂Se₃ (001) plane is analogous with that of the honeycomb match between CdS (100) and Bi₂Se₃ (100) (Figure S25d). The addition of PbS NPs exhibits our ability to incorporate different symmetry and potential functionality in this synthetic system.

The rational control of 2D NHS synthesis gives us the opportunity to further investigate the functionality and device applications of these unique material systems. We use photoelectrochemical cells (PECs) to test the performance of the as-synthesized Bi₂Se₃–CdS NHSs, in which the photo ($\lambda > 420$ nm) oxidation of a Na₂SO₃/Na₂S aqueous solution is chosen as the photoanodic reaction.²⁷ The single compositional materials of CdS and Bi₂Se₃ are used individually in our control experiments and show relatively low anodic photocurrent density of 0.059 and 0.003 mA/cm² at the onset potential (where the dark current is zero) (–0.9 V vs SCE), respectively. This value for the basal NHS (sample 2–4) reaches 0.11 mA/cm² (–0.9 V vs SCE), which is much higher than single constituents (Figure 3a,b). Significantly, the anodic photocurrent density of the lateral Bi₂Se₃–CdS NHS (sample 2–2) show the highest value of 0.19 mA/cm² (–0.9 V vs SCE), surpassing the single compositional materials and the basal NHS (Figure 3a and b). Electrochemical impedance spectra (EIS) (Figure 3c and Figure S26d) reveals that the charge transfer at the electrode–solution interface is dramatically improved in the NHS.²⁸ The incident photon to current efficiency (IPCE) spectra also agree well with the photocurrent values that the NHS has much higher photoresponse than single components (Figure 3f). The trend in the photocurrents is further verified with the photocatalytic degradation of methyl orange (Figure S26e).

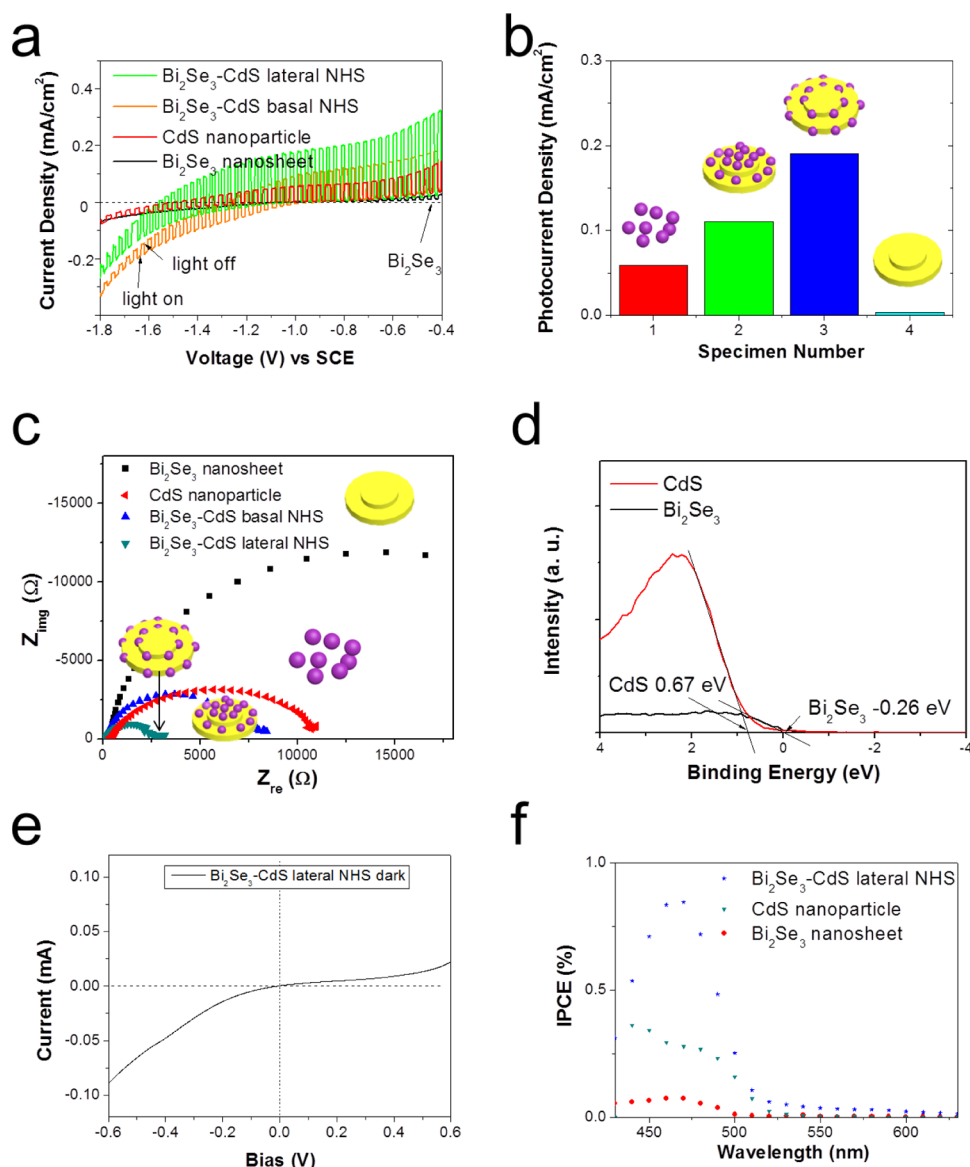


Figure 3. (a) J-V plots under on-off switch of light, (b) photocurrent density values at -0.9 V vs SCE, (c) Nyquist plots of different samples: 1, CdS NPs; 2, basal (vertical) Bi₂Se₃-CdS NHS (sample 2-4); 3, lateral Bi₂Se₃-CdS NHS (sample 2-2); and 4, Bi₂Se₃ NSs, (d) XPS valence spectra of CdS NPs and Bi₂Se₃ NSs, (e) dark I-V plot of lateral Bi₂Se₃-CdS NHS sample 2-2 showing rectification, and (f) IPCE spectra of different samples.

We believe the boost of performances in the NHSs might originate from the Bi₂Se₃-CdS heterojunction that facilitated the charge separation upon illumination²⁸ and perform both the experimental and theoretical studies to verify this hypothesis. XPS valence spectra and band gap data (Figure 3d and Figure S27) indicate that the conduction-band minimum (CBM) of CdS is higher than that of Bi₂Se₃ by 0.66 eV, leading to the possibility of electron transfer²⁹ from CdS to Bi₂Se₃ in the NHS. Meanwhile, as indicated by DFT calculation, some interface states reflecting electron coupling between Bi₂Se₃ and CdS in the NHS are present in the vicinity of CBM (Figure 4 and Figure S29a-d), as a strong indication of electron transfer channels from CdS to Bi₂Se₃. The intrinsic properties of Bi₂Se₃ NSs that special surface states fall within the bulk energy gap¹⁸ allow the injected photogenerated electrons to rapidly move far from the interface by the conductive metallic basal planes of Bi₂Se₃. At the same time, near the valence band maximum (VBM), the bands of Bi₂Se₃ and CdS contributing to photogenerated holes remain uncoupled (Figure S29e-h).

Thus, under illumination, the photogenerated electrons in CdS can migrate to Bi₂Se₃, while the photogenerated holes will remain in the CdS itself. As a result, the electron-hole spatial separation is achieved in the NHS. In addition, relative to finite-size CdS NPs, the 2D Bi₂Se₃ serves as the electron reservoir, continuously accepting the photogenerated electrons and simultaneously leaving the same number of photogenerated holes in the CdS. Furthermore, the asymmetric I-V plot and rectification of the currents (Figure 3e (dark) and Figure S26b (under illumination)) have been observed, again suggesting that there is a charge separation in our NHS under illumination due to the existence of heterojunction.³⁰ The enhanced charge-carrier spatial separation might increase the photocurrent of our lateral NHS-based PEC, which corresponds to the significant increase of carrier (electrons and holes) concentration upon illumination.²⁸ By contrast, only a weak electron coupling exists in the basal NHS with the vdW interaction, which yields a moderate improvement in performance.

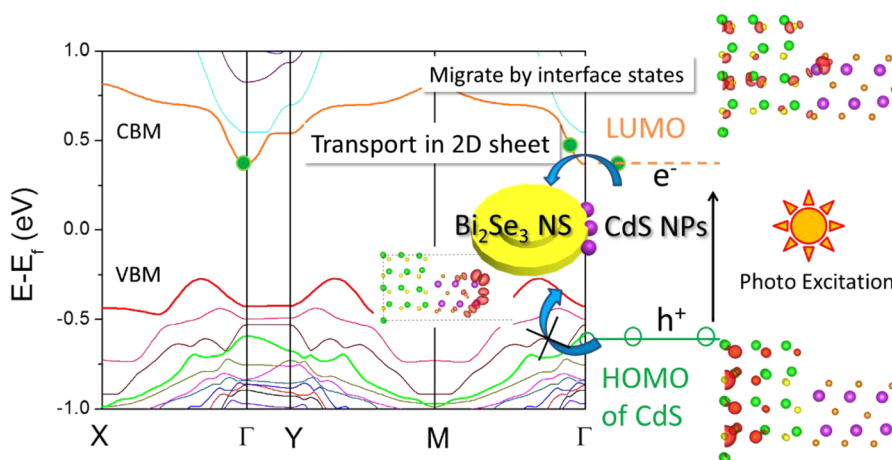


Figure 4. Scheme of principle of the charge separation in lateral Bi_2Se_3 – CdS NHS based on band structure of Bi_2Se_3 and HOMO–LUMO of CdS from DFT calculations. In the atomic models, the green atoms stand for Cd, yellow for S, purple for Bi, and orange for Se. The red bubbles stand for the isosurface of the squared wave function.

In conclusion, we have achieved the selective synthesis of lateral and basal NHSs using Bi_2Se_3 and CdS through understanding the binding thermodynamics and regulating the reaction kinetics. On the basis of the insights into the interfacial bonding, this synthetic system has been extended to other metal chalcogenides. The lateral 2D NHS shows excellent performance in a photoelectrochemical cell application as compared to the basal counterpart due to the electronic structures yielded from unique structure-dependent chemical and physical properties. This study elucidates that the site-related differences stem from the bonding feature of 2D materials and sensitivity to the reaction kinetics. This finding will inspire the controllable site-selective fabrication of 2D NHS with tunable functionalities.

■ ASSOCIATED CONTENT

Supporting Information

Experimental details, structural characterizations on Bi_2Se_3 – CdS NHSs, details on DFT modeling, structural characterizations on extended synthetic system, and detailed data on photoelectrochemical cells. The Supporting Information is available free of charge on the ACS Publications website at DOI: 10.1021/acs.nanolett.5b01464.

■ AUTHOR INFORMATION

Corresponding Authors

*E-mail: yuewu@iastate.edu.

*E-mail: wangxun@mail.tsinghua.edu.cn.

Author Contributions

B.X. and H.L. contributed equally. The manuscript was written through contributions of all authors. All authors have given approval to the final version of the manuscript.

Notes

The authors declare no competing financial interest.

■ ACKNOWLEDGMENTS

This work was supported by NSFC (21431003, 91127040, 21221062), the State Key Project of Fundamental Research for Nanoscience and Nanotechnology (2011CB932402), National Basic Research Program of China (2014CB932101), and the startup funding from Iowa State University.

■ REFERENCES

- (1) Novoselov, K. S.; Geim, A. K.; Morozov, S. V.; Jiang, D.; Zhang, Y.; Dubonos, S. V.; Grigorieva, I. V.; Firsov, A. A. *Science* **2004**, *306*, 666–669.
- (2) Geim, A. K.; Novoselov, K. S. *Nat. Mater.* **2007**, *6*, 183–191.
- (3) Chhowalla, M.; Shin, H. S.; Eda, G.; Li, L. J.; Loh, K. P.; Zhang, H. *Nat. Chem.* **2013**, *5*, 263–275.
- (4) Huang, X.; Tan, C.; Yin, Z.; Zhang, H. *Adv. Mater.* **2014**, *26*, 2185–2204.
- (5) Banin, U.; Ben-Shahar, Y.; Vinokurov, K. *Chem. Mater.* **2013**, *26*, 97–110.
- (6) Macdonald, J. E.; Bar Sadan, M.; Houben, L.; Popov, I.; Banin, U. *Nat. Mater.* **2010**, *9*, 810–815.
- (7) Kempa, T. J.; Kim, S.-K.; Day, R. W.; Park, H.-G.; Nocera, D. G.; Lieber, C. M. *J. Am. Chem. Soc.* **2013**, *135*, 18354–18357.
- (8) Geim, A. K.; Grigorieva, I. V. *Nature* **2013**, *499*, 419–425.
- (9) Hong, Y. J.; Yang, J. W.; Lee, W. H.; Ruoff, R. S.; Kim, K. S.; Fukui, T. *Adv. Mater.* **2013**, *25*, 6847–6853.
- (10) Björkman, T.; Gulans, A.; Krashenninnikov, A. V.; Nieminen, R. M. *Phys. Rev. Lett.* **2012**, *108*, 235502.
- (11) Jaramillo, T. F.; Jorgensen, K. P.; Bonde, J.; Nielsen, J. H.; Horch, S.; Chorkendorff, I. *Science* **2007**, *317*, 100–102.
- (12) Jeon, I.-Y.; Choi, H.-J.; Jung, S.-M.; Seo, J.-M.; Kim, M.-J.; Dai, L.; Baek, J.-B. *J. Am. Chem. Soc.* **2012**, *135*, 1386–1393.
- (13) Cervantes-Sodi, F.; Csányi, G.; Piscanec, S.; Ferrari, A. C. *Phys. Rev. B* **2008**, *77*, 165427.
- (14) Liu, L.; Park, J.; Siegel, D. A.; McCarty, K. F.; Clark, K. W.; Deng, W.; Basile, L.; Idrobo, J. C.; Li, A.-P.; Gu, G. *Science* **2014**, *343*, 163–167.
- (15) Duan, X.; Wang, C.; Shaw, J. C.; Cheng, R.; Chen, Y.; Li, H.; Wu, X.; Tang, Y.; Zhang, Q.; Pan, A.; Jiang, J.; Yu, R.; Huang, Y.; Duan, X. *Nat. Nanotechnol.* **2014**, *9*, 1024–1030.
- (16) Kong, D.; Cui, Y. *Nat. Chem.* **2011**, *3*, 845–849.
- (17) Xia, Y.; Qian, D.; Hsieh, D.; Wray, L.; Pal, A.; Lin, H.; Bansil, A.; Grauer, D.; Hor, Y. S.; Cava, R. J.; Hasan, M. Z. *Nat. Phys.* **2009**, *5*, 398–402.
- (18) Zhang, H.; Liu, C.-X.; Qi, X.-L.; Dai, X.; Fang, Z.; Zhang, S.-C. *Nat. Phys.* **2009**, *5*, 438–442.
- (19) Li, H.; Wang, X.; Xu, J.; Zhang, Q.; Bando, Y.; Golberg, D.; Ma, Y.; Zhai, T. *Adv. Mater.* **2013**, *25*, 3017–3037.
- (20) Min, Y.; Moon, G. D.; Kim, B. S.; Lim, B.; Kim, J.-S.; Kang, C. Y.; Jeong, U. *J. Am. Chem. Soc.* **2012**, *134*, 2872–2875.
- (21) Shen, S.; Zhang, Y.; Peng, L.; Xu, B.; Du, Y.; Deng, M.; Xu, H.; Wang, Q. *CrystEngComm* **2011**, *13*, 4572–4579.
- (22) Zhang, J.; Peng, Z.; Soni, A.; Zhao, Y.; Xiong, Y.; Peng, B.; Wang, J.; Dresselhaus, M. S.; Xiong, Q. *Nano Lett.* **2011**, *11*, 2407–2414.

- (23) Kostić, R.; Romčević, N. *Phys. Status Solidi C* **2004**, *1*, 2646–2649.
- (24) Gutzow, I. S. *The Vitreous State: Thermodynamics, Structure, Rheology, and Crystallization*; Springer: Berlin, Germany, 1995.
- (25) Schmelzer, J. *Nucleation Theory and Applications*; WILEY-VCH Verlag GmbH & Co. KGaA: Weinheim, Germany, 2005.
- (26) Mullin, J. W. *Crystallization*; Butterworth–Heinemann: Oxford, U.K., 2001.
- (27) Yang, J.; Yan, H.; Wang, X.; Wen, F.; Wang, Z.; Fan, D.; Shi, J.; Li, C. *J. Catal.* **2012**, *290*, 151–157.
- (28) Kim, E. S.; Nishimura, N.; Magesh, G.; Kim, J. Y.; Jang, J.-W.; Jun, H.; Kubota, J.; Domen, K.; Lee, J. S. *J. Am. Chem. Soc.* **2013**, *135*, 5375–5383.
- (29) Shen, H.; Jiao, X.; Oron, D.; Li, J.; Lin, H. *J. Power Source* **2013**, *240*, 8–13.
- (30) Hou, Y.; Li, X.-Y.; Zhao, Q.-D.; Quan, X.; Chen, G.-H. *Adv. Funct. Mater.* **2010**, *20*, 2165–2174.